



Pulsed laser deposition and annealing of $\text{Bi}_{2-x}\text{Sb}_x\text{Te}_3$ thin films for *p*-type thermoelectric elements

Jane E. Cornett^a, Oded Rabin^{a,b,*}

^a Department of Materials Science and Engineering, University of Maryland, College Park, MD 20742, USA

^b Institute for Research in Electronics and Applied Physics, University of Maryland, College Park, MD 20742, USA

ARTICLE INFO

Article history:

Available online 14 July 2014

The review of this paper was arranged by Prof. A. Zaslavsky

Keywords:

Thermoelectrics

Pulsed laser deposition

Bi_2Te_3

$\text{Bi}_{2-x}\text{Sb}_x\text{Te}_3$

Vapor anneal

Non-stoichiometric compound

ABSTRACT

Pulsed laser deposition is suggested as a convenient method for fabrication of $\text{Bi}_{2-x}\text{Sb}_x\text{Te}_3$ thin films for *p*-type thermoelectric elements. However, challenges with controlling the stoichiometry and the microstructure of the films need to be addressed. Annealing of the films in an environment of nitrogen and tellurium vapor provided a means to producing $\text{Bi}_{2-x}\text{Sb}_x\text{Te}_3$ thin films with power factor values similar or greater than bulk materials. Films deposited at 2 mTorr, 375 °C with a laser power of 1.6 W were metal-rich and disordered, with small negative Seebeck coefficients. Upon annealing these films become single phase with a stoichiometry close to 2:3, textured with the basal plane parallel to the substrate, and exhibit excellent *p*-type thermoelectric characteristics. Interestingly, using this particular deposition and annealing sequence no secondary phases (e.g. crystalline tellurium) are formed.

© 2014 Elsevier Ltd. All rights reserved.

1. Introduction

Thin films of thermoelectric materials are of interest for embedded thermal management and waste energy harvesting systems within electronic devices. This paper describes the use of pulsed laser deposition (PLD) to obtain thin films of $\text{Bi}_{2-x}\text{Sb}_x\text{Te}_3$ ($x \sim 1.5$), a room temperature thermoelectric material. The composition, microstructure and thermoelectric properties of $\text{Bi}_{2-x}\text{Sb}_x\text{Te}_3$ thin films are very sensitive to fabrication conditions due to the high vapor pressure of Te and the existence of many stoichiometric and non-stoichiometric compounds in the Bi–Sb–Te system.

1.1. $\text{Bi}_{2-x}\text{Sb}_x\text{Te}_3$ materials system

The $\text{Bi}_{2-x}\text{Sb}_x\text{Te}_3$ materials system is one of the best known room temperature *p*-type thermoelectric materials [2]. The compounds show high values of thermoelectric power factor *PF* (the product of the electrical conductivity and the square of the Seebeck coefficient) and high dimensionless thermoelectric figure-of-merit *ZT* (the product of the power factor, the temperature and the inverse of the thermal conductivity), that reach a maximum for compositions with atomic ratio Sb:Bi $\sim 3:1$. The excellent thermoelectric properties of $\text{Bi}_{2-x}\text{Sb}_x\text{Te}_3$ can be largely attributed to its complex

crystal structure. Bi_2Te_3 , Sb_2Te_3 and the alloy $\text{Bi}_{2-x}\text{Sb}_x\text{Te}_3$ are described by a rhombohedral unit cell, or by a hexagonal primitive cell with layers of metal and chalcogenide atoms perpendicular to the [0001] direction (see Fig. 1). The hexagonal primitive cell consists of three quintets (5 layers each). Each quintet has the form Te(1)–Bi/Sb–Te(2)–Bi/Sb–Te(1). The Bi/Sb–Te bonds have mixed ionic and covalent character, while the Te(1)–Te(1) bonds between quintets are Van der Waals and are therefore much weaker. The room temperature hexagonal lattice parameters for Bi_2Te_3 and Sb_2Te_3 are given in Table 1. The lattice parameter *a* follows Vegard's law ($a_{\text{Bi}_{2-x}\text{Sb}_x\text{Te}_3} = \frac{(2-x)}{2}a_{\text{Bi}_2\text{Te}_3} + \frac{x}{2}a_{\text{Sb}_2\text{Te}_3}$), decreasing as the alloy becomes more Sb-rich. The change in lattice parameter *c* with alloying is not well-documented, with some reports indicating almost no dependence on the Sb:Bi ratio [3,4] and other reports indicating that *c* is actually lower for alloys than for either Bi_2Te_3 or Sb_2Te_3 [5].

The high-symmetry rhombohedral crystal structure translates to a sixfold degeneracy of the valence and conduction bands [6]. This kind of high band degeneracy is beneficial to the thermoelectric power factor: The total electrical conductivity increases by a factor of ~ 6 relative to the non-degenerate band without negatively impacting the Seebeck coefficient. Furthermore, the complex crystal structure, the large mass of the atoms and alloy disorder of $\text{Bi}_{2-x}\text{Sb}_x\text{Te}_3$ lead to low values of the thermal conductivity [7]. The high power factor and the low thermal conductivity contribute to a high thermoelectric figure-of-merit in $\text{Bi}_{2-x}\text{Sb}_x\text{Te}_3$ alloys.

* Corresponding author at: Department of Materials Science and Engineering, University of Maryland, College Park, MD 20742, USA. Tel.: +1 301 405 3382.

E-mail address: oded@umd.edu (O. Rabin).

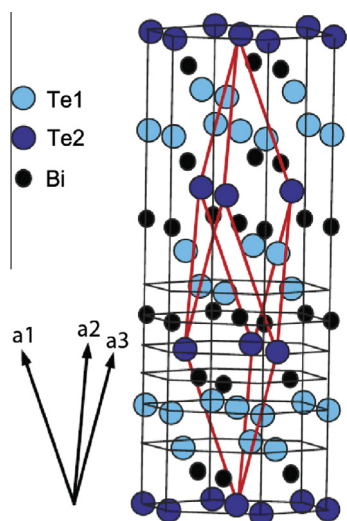


Fig. 1. Hexagonal primitive cell of Bi_2Te_3 . The rhombohedral unit cell is marked in red, with lattice vectors shown at the bottom left. Adapted from [1].

Table 1
Hexagonal lattice parameters for Bi_2Te_3 and Sb_2Te_3 at 300 K [2].

Compound	a (nm)	c (nm)
Bi_2Te_3	0.43835	3.0360
Sb_2Te_3	0.4275	3.0490

Reported literature values for the electrical and thermal conductivities and the Seebeck coefficient of p -type Bi_2Te_3 , Sb_2Te_3 and $\text{Bi}_{0.5}\text{Sb}_{1.5}\text{Te}_3$ are given in Table 2. These values were measured in the hexagonal basal plane (perpendicular to the c -direction). The ZT value for Sb_2Te_3 is far less than 1, thus too low for practical application. Alloying with Bi_2Te_3 both increases the power factor and substantially decreases the lattice thermal conductivity as the result of phonon scattering due to alloy disorder.

1.2. Pulsed laser deposition of $\text{Bi}_{2-x}\text{Sb}_x\text{Te}_3$ -type materials

The first report of Bi_2Te_3 thin films produced via pulsed laser deposition was published in 1996 [11]. In this work, Dauscher et al. found that the deposited film is Te-deficient at positions close to the incoming laser, as the laser interacts with the plasma plume coming off the target [11]. Subsequent studies of PLD as a means for depositing Bi_2Te_3 -based thin films led to significant improvement in terms of the properties of the deposited films. In 2007, Bailini et al. reported excellent control over the morphology of n -type Bi_2Te_3 films by varying the background Ar pressure and the substrate temperature [12]. The deposited films vary from disordered and nanocrystalline (room temperature) to highly-textured (high temperature, high pressure). The highest in-plane power factor

Table 2
Room temperature transport properties of p -type Bi_2Te_3 , Sb_2Te_3 and $\text{Bi}_{0.5}\text{Sb}_{1.5}\text{Te}_3$.

Compound	Electrical conductivity (S/m)	Seebeck coefficient ($\mu\text{V/K}$)	Thermal conductivity (W/m K)	ZT
Bi_2Te_3 [8]	1.0×10^5	190	2	0.54
Sb_2Te_3 [9]	4.7×10^5	79	5	0.18
$\text{Bi}_{0.5}\text{Sb}_{1.5}\text{Te}_3$ [10]	8.7×10^4	230	1.4	0.99

values reported by this group ($\sim 2\text{--}5 \times 10^{-3} \text{ W/m K}^2$ at room temperature) are found for textured films deposited at 10 Pa and temperatures between 250 and 350 °C [13]. In 2003, Makala et al. reported the first successful pulsed laser deposition of $\text{Bi}_{2-x}\text{Sb}_x\text{Te}_3$ thin films. They found extremely low thermal conductivities (0.3–0.4 W/m K) in films deposited from an $x = 1.5$ alloy target onto both mica and AlN/Si (100) substrates. However, high defect densities and issues with controlling stoichiometry led to low conductivity values and low room temperature ZT values (0.05–0.08) [14]. Obara et al. later demonstrated $x = 1.7$ alloy films with high room temperature power factor values ($3.7 \times 10^{-3} \text{ W/m K}^2$), attributed to good control over stoichiometry [15]. These results indicate that while PLD is a promising technique for deposition of $\text{Bi}_{2-x}\text{Sb}_x\text{Te}_3$ thin films, preventing loss of Te during deposition and annealing is crucial to achieve electrical transport values comparable with bulk.

We report on the characteristics of $\text{Bi}_{2-x}\text{Sb}_x\text{Te}_3$ films deposited by PLD as a function of deposition conditions. The effects of substrate temperature, background pressure and laser power on the pulsed laser deposited thin films were investigated. Subsequently, the effect of annealing in N_2 gas and Te vapor on the properties of the films was examined. Annealing is necessary in order to recover crystalline films; however, careful optimization of the annealing conditions (temperature, pressure, background gas chemistry) is needed in order to prevent loss of highly volatile Te. The fabrication of the $\text{Bi}_{2-x}\text{Sb}_x\text{Te}_3$ films was carried out in a custom-made PLD vacuum chamber that facilitated *in situ* post-deposition annealing with control over gas pressure and chemistry as well as substrate temperature.

2. Experimental methods

2.1. Deposition chamber

$\text{Bi}_{2-x}\text{Sb}_x\text{Te}_3$ films were grown by PLD in a custom-built pulsed-laser deposition and thermal evaporation co-deposition system (BlueWave Semiconductors Inc.). The PLD-thermal evaporation system can accommodate 3 targets for PLD and 2 boats for thermal evaporation. The $\sim 1 \text{ m}^3$ chamber is evacuated to $\sim 10^{-3}$ Torr with a Pfeiffer DUO035 roughing pump. High vacuum ($<10^{-6}$ Torr) is achieved with a Pfeiffer HiPace 400 turbo pump. A gate valve separates the main deposition chamber from the pumping stack. The pressure is measured using a Pfeiffer PKR251 Compact FullRange Gauge (10^{-9} – 10^{-2} Torr). The pressure is controlled manually using the turbo pump, the roughing pump and N_2 gas flow controlled using an MKS Mass Flow Controller and a 167 Readout/Set Point Module. Pressures between 10^{-3} Torr and 2 Torr are obtained with the turbo pump off, the roughing pump on and a gas load between 1 and 100 sccm. For pressures between 10^{-6} Torr and 10^{-3} Torr, the turbo pump is set to “standby mode” (at 65% max. spinning speed) and the gas flow to between 1 and 40 sccm.

Fig. 2 shows the arrangement of components inside the chamber. Substrates up to 2" in diameter are mounted onto the sample holder, facing down. The holder can be moved up and down within the chamber and it can rotate. The temperature of the substrate is monitored and controlled with a Eurotherm 2416 Controller/Programmer connected to a heater and a calibrated thermocouple inside the substrate holder.

Pulsed laser deposition is performed using the second harmonic of a Nd:YAG Quantel Brilliant b laser ($\lambda = 532 \text{ nm}$, $\tau = 4 \text{ nsec}$, $f = 10 \text{ Hz}$). The laser beam is routed by a set of high damage-threshold mirrors and focused onto the PLD targets by a lens on a cage mount. Targets are loaded onto a motorized carousel for target selection and rotation. A stainless steel cover exposes one target at a time and reduces cross-contamination.

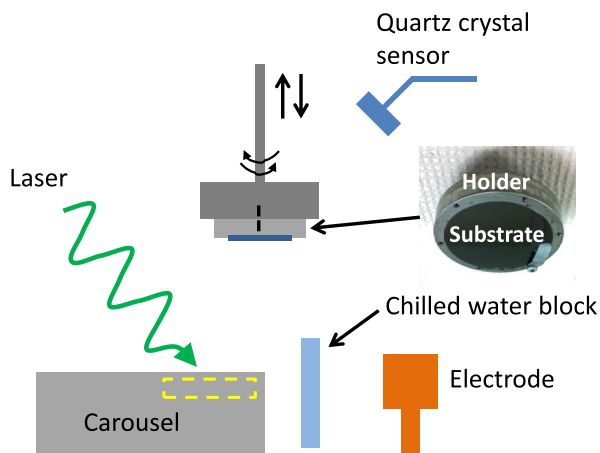


Fig. 2. Schematic of arrangement of the components inside the deposition chamber, viewed from the front.

Three water-cooled copper electrode feed-throughs accommodate two $\sim 10\text{ cm} \times 1\text{ cm}$ evaporation boats with a common ground. An INFICON SQC-310 Thin Film Deposition Controller is used to control the deposition rate and final thickness of the films deposited by thermal evaporation (rate resolution: 0.01 \AA/sec). Two shutters (not shown in Fig. 2) are used to cover the substrate and the evaporation boats, respectively, when appropriate. To prevent cross-contamination, the electrodes for thermal evaporation are separated from the target carousel by a water-cooled barrier.

2.2. Film deposition and annealing conditions

The substrate was typically a $20\text{--}30\text{ }\Omega\text{ cm}$ resistivity $\langle 100 \rangle$ Si wafer (Silicon Inc.) with the native oxide intact, $\sim 15 \times 30\text{ mm}^2$ in size. The chamber was evacuated to a base pressure of $\sim 10^{-6}$ Torr prior to deposition and backfilled with N_2 to achieve background pressures between 2×10^{-3} and 2 Torr. The substrate temperature was varied between 25° and $\sim 375^\circ\text{C}$. The Nd:YAG laser was focused onto a rotating $\text{Bi}_{0.5}\text{Sb}_{1.5}\text{Te}_3$ target (American Elements, Merelex Corp.) with an average power between 0.6 and 3.6 W (energy densities between 3 and $18\text{ J/cm}^2/\text{pulse}$). Prior to deposition, the PLD target was cleaned (with the substrate covered by a

shutter) by ablating for 1 min at the desired laser power. The depositions were 26 min long; with the substrate $\sim 4\text{ cm}$ from the target, the deposited films were $100\text{--}250\text{ nm}$ thick giving a deposition rate between 0.06 and 0.16 nm/s .

For the annealing in nitrogen, all films were deposited on $\langle 100 \rangle$ Si with a laser power of 1.6 W and a deposition pressure of 2 mTorr. Immediately after deposition, the temperature was increased from 375 to 390°C and the N_2 flow was increased to reach a chamber pressure of 2 Torr. The films were annealed at this temperature and pressure (for up to 17 h) and then cooled to room temperature under 2 Torr of N_2 . For the annealing in nitrogen with Te vapor, an alumina-coated molybdenum boat (Kurt Lesker) loaded with 99.999% Te pellets (Sigma-Aldrich) was connected to the thermal evaporation electrodes. Immediately after deposition, the temperature of the substrate was increased to 390°C and the substrate was moved upwards to a distance of 20 cm from the evaporation boat. Annealing was done at the same pressure as the deposition (2 mTorr). The power to the evaporation electrodes was set manually and held constant (at $\sim 60\text{ mW}$), and the rate of Te deposition read on the Inficon Deposition Controller was less than 0.01 \AA/sec (undetermined). The low flux of Te and the high temperature of the substrate prevent the deposition of tellurium as a thin film on the substrate.

An example of the pressure and temperature profiles before, during and after typical depositions is given in Fig. 3.

2.3. Characterization

The morphology of the deposited films was determined using a Hitachi SU-70 Analytical Scanning Electron Microscope (SEM) operated at 10 kV . The crystal structure of the thin films was characterized by X-ray diffraction (XRD) using a Bruker D8 Advance system ($\text{Cu K}\alpha$ radiation). 2θ values between 15° and 65° were scanned with a rate of $0.7^\circ/\text{min}$.

Preliminary analysis of the film composition was done using a Bruker Energy-Dispersive X-ray Detector attached to the SEM. However, due to errors in the measurement of small amounts of Bi and Sb on Si substrates, more accurate measurements of the composition of the films were done using a Perkin-Elmer 4300 Inductively Coupled Plasma Optical Emissions Spectrometer (ICP-OES). Calibration standards for Bi, Sb and Te were made by dissolving bismuth citrate ($\text{C}_6\text{H}_5\text{BiO}_7$), antimony oxide (Sb_2O_3) and tellurium oxide (TeO_2) (all purchased from Alfa Aesar) in an aqueous 10% wt nitric acid, 1.5% wt tartaric acid solution.

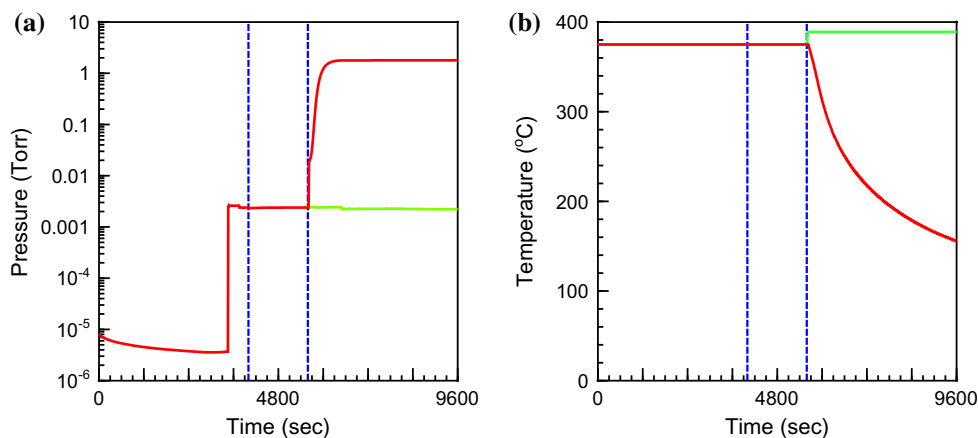


Fig. 3. Example of the recorded (a) pressure and (b) temperature as a function of time before, during and after two depositions (red solid line: without anneal step; green solid line: with N_2/Te anneal step). The 2 dashed vertical lines mark the times of the start of the deposition and the end of the deposition. (For interpretation of the references to color in this figure legend, the reader is referred to the web version of this article.)

Standards of 100–1000 ppb ($\mu\text{g/L}$) were made for each element. Samples ($\sim 3 \times 3 \text{ mm}^2$ pieces of the deposited films on Si) were digested in $\sim 1 \text{ mL}$ of 70% wt nitric acid. Once completely dissolved (after $\sim 1 \text{ h}$), tartaric acid and deionized water were added to match the matrix solution of the standards. Based on measurement of standard solutions with similar concentrations, we estimate the average error in the measurement of each element to be $<2\%$ at.

The room temperature transport properties of the films (sheet resistance and Seebeck coefficient) were measured in a Signatone S1160 probe station using established methods. The sheet resistance of the thin films was measured by the van der Pauw method on rectangle-shaped specimens (Keithley 6221 current source and Keithley 2182A nanovoltmeter). The conductivity values were then calculated using film thicknesses measured by cross-sectional SEM. For most PLD runs, we find that the film thickness varies by $\sim 10\%$ over the entire substrate, corresponding to the largest uncertainty in determining the electrical conductivity. The Seebeck coefficient was measured using the “two-thermocouple” method described in [16]. A temperature gradient was generated by passing current through a $1 \text{ k}\Omega$ flat resistor positioned flush with one edge of the sample. Two $0.005''$ -thick foil Type E thermocouples (Omega Engineering) were placed in electrical and thermal contact with the thin film at two locations. Voltages across the n -type legs and the p -type legs were measured with a Keithley 2182A nanovoltmeter. In a typical measurement the heating current was repeatedly cycled in steps between 10 and 40 mA, resulting in a ΔT of 0.5 – 4°C across the sample, while the average temperature increased less than 30°C above room temperature throughout the measurement. In each sample measurement, the Seebeck coefficient typically varies by $<10\%$ for the range of ΔT specified. The reported Seebeck coefficient of the film is an average over the values from the entire measurement (the range of ΔT and of the sample temperature). It is noted that a 2-point resistance less than $20 \text{ k}\Omega$ between the thermocouples guaranteed a stable measurement. The room temperature Seebeck coefficients of Type E thermocouple legs (chromel and constantan) are $S_{\text{chromel}} = 22.4 \mu\text{V/K}$ and $S_{\text{constantan}} = -38.1 \mu\text{V/K}$.

Hall Effect measurements were done using a HMS-5000 Hall Effect Measurement System, equipped with a 0.51 T magnet.

3. Results and discussion

3.1. Effect of deposition conditions

3.1.1. Effect of substrate temperature

SEM images of films deposited with a laser power of 0.6 W at 90 mTorr for substrate temperatures between 25° and 375°C are shown in Fig. 4. In general, we see sintering and growth of grains in the as-deposited films as the substrate temperature increases. For a substrate temperature of less than 375°C , XRD results indicate that the films are amorphous. These amorphous films typically exhibit conductivity values $<10^2 \text{ S/m}$, far below the literature value for $\text{Bi}_{0.5}\text{Sb}_{1.5}\text{Te}_3$ (Table 2). Based on these results, subsequent depositions were all done with a high substrate temperature of 375°C .

3.1.2. Effects of background pressure and laser power

The effects of the background gas pressure and the laser power on films deposited on $\langle 100 \rangle$ Si with a substrate temperature of 375°C was studied. Depositions were done at pressures of 2, 90, 180, 310, 590 and 1900 mTorr and time-average laser powers of 0.6, 0.9, 1.2, 1.4, 1.6 and 3.1 W . The background gas was ultra high purity nitrogen (Airgas).

The morphologies of the deposited films were compared by top-surface SEM imaging. Images of films deposited within this pressure-power parameter space are shown in Fig. 5. The film roughness and the contrast between grains increases with both deposition pressure and laser power. However, an increase in deposition pressure also corresponds to a change in film thickness, while no such trend is clear with laser power. Low pressure (2 mTorr) depositions yield extremely smooth and thin films (typically $<100 \text{ nm}$ thick). For high deposition pressures ($>200 \text{ mTorr}$), the deposited film can have a pillared morphology: This is observed in the top-surface and cross-sectional SEM images (Fig. 5, $P = 1900 \text{ mTorr}$ and Fig. 6, 590 mTorr). In addition to this interesting microstructure, high deposition pressures also

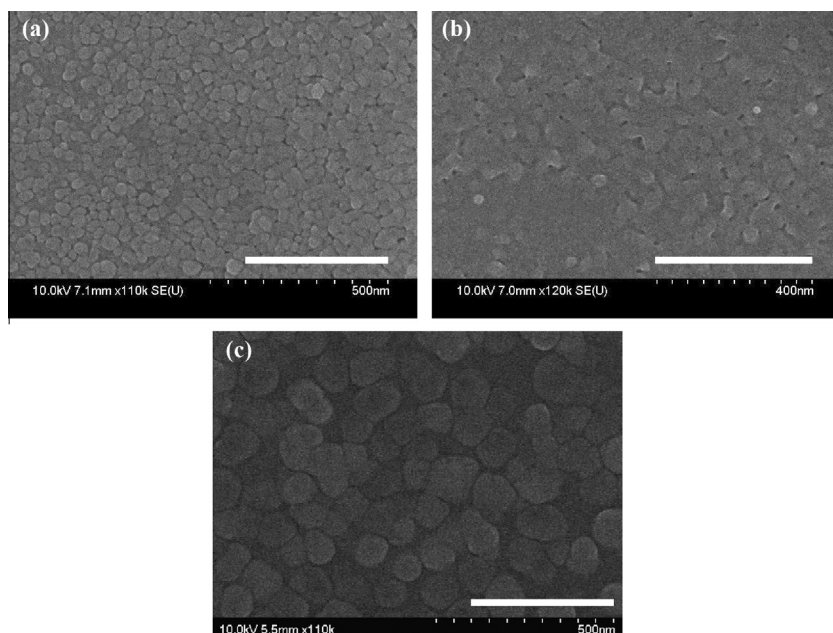


Fig. 4. Top surface SEM images of films deposited at 0.6 W , 90 mTorr with substrate temperatures of (a) 25°C , (b) 100°C and (c) 375°C . All depositions were 26 min long. All images were taken at 110–120 kx magnification (scale bar: 400 nm).

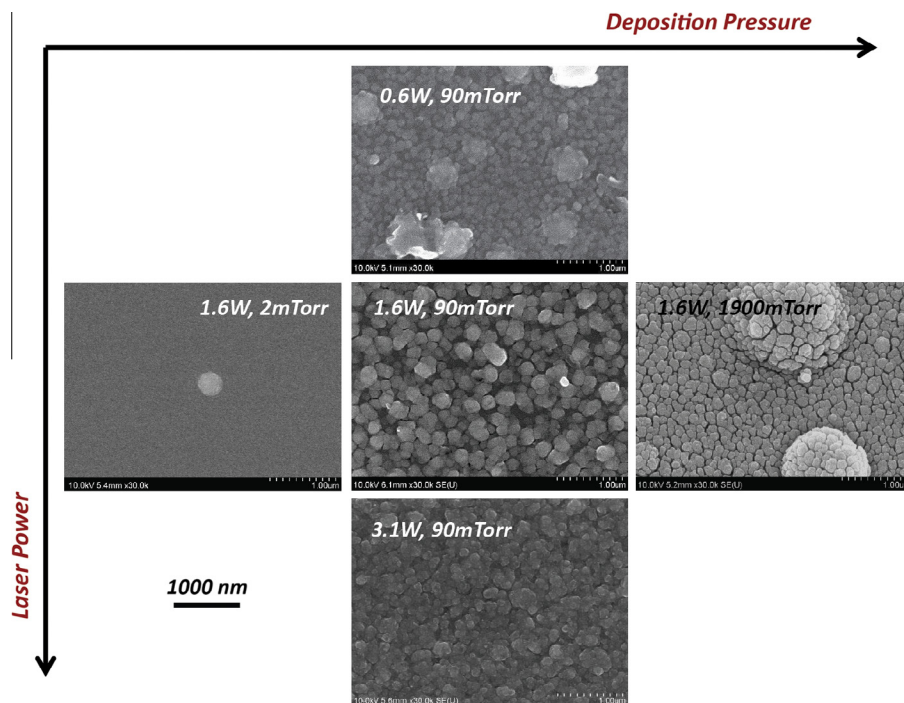


Fig. 5. SEM images of films deposited at various pressures with various laser powers. All depositions were 26 min long, and the substrate temperature was 375 °C. All images taken at a magnification of 30 kx (scale bar: 1000 nm).

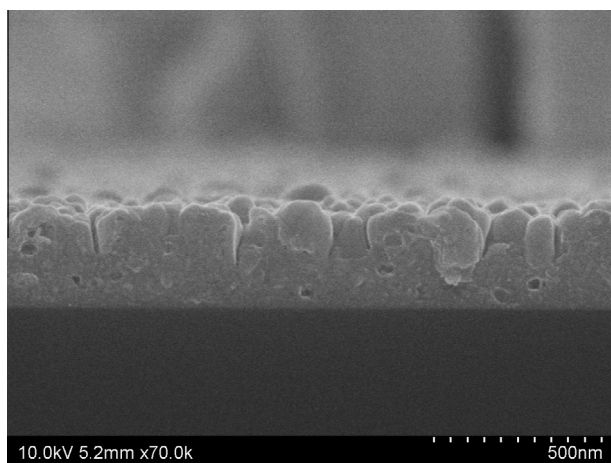


Fig. 6. Cross-sectional SEM image of a film with a nanopillar morphology. The film was deposited at 1.6 W, 590 mTorr.

generally lead to a strong and visible thickness gradient over the substrate area.

Examples of XRD spectra from films deposited within this range of conditions are shown in Fig. 7. In general, low laser powers and low deposition pressures yield disordered films characterized by broad peaks (see spectrum for 1.6 W, 2 mTorr deposition). Crystalline films are achieved for higher powers and pressures. However, high pressure and high power deposition conditions typically result in the formation of mixtures of crystalline phases, including Bi_2Te_3 , Sb_2Te_3 , Sb-rich alloy and/or Te (see Fig. 7(b)). Separate Bi_2Te_3 and Sb_2Te_3 phases yield separate (015) peaks in the XRD spectrum because (as explained in Section 1.1) the a lattice parameter for these two materials is different. Separate peaks are not observed for (00 l) reflections, however, because the c lattice parameters for Bi_2Te_3 and Sb_2Te_3 differ by only 0.4%.

The EDX spectrometer in the SEM was used to determine the effect of laser power and pressure on thin film composition. Values

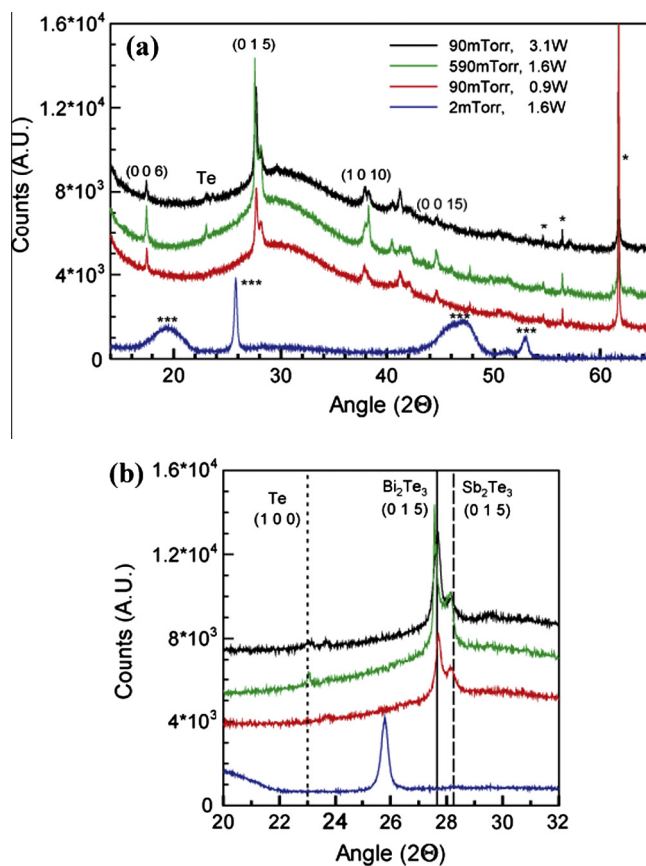


Fig. 7. XRD spectra for films deposited with laser powers between 0.9 and 3.1 W at pressures between 2 and 590 mTorr. The traces were offset for clarity. Peaks marked by * are from the Si substrate. Peaks marked by *** are from a disordered $(\text{Bi,Sb})_{x-y}\text{Te}_y$ phase ($x:y \neq 2:3$). The peaks from (015) planes for Bi_2Te_3 and Sb_2Te_3 (JCPDS 015-0863 and 015-0874) are marked by solid and dashed black lines in (b). The (100) Te peak (JCPDS 036-1453) is seen in several of the spectra.

of the metal-to-tellurium (M:Te = (Bi + Sb):Te) and Sb:Bi atomic ratios for the range of deposition pressures and laser powers investigated here are given in Tables 3 and 4, respectively.

Table 3

M:Te atomic ratios from EDX measurements of as-deposited films. The target value is 0.67.

		Deposition pressure (mTorr)					
		2	90	180	310	590	1900
Laser power (W)	0.6	1.72	0.75				
	0.9		1.09				
	1.2	1.25	0.95	0.64	1.34	1.34	2.09
	1.4	1.22	0.70	0.66	0.73	1.08	1.43
	1.6	1.15	0.83	0.59		0.77	1.12
	3.1		0.58				

Table 4

Sb:Bi atomic ratios from EDX measurements of as-deposited films. The target value is 3.

		Deposition pressure (mTorr)					
		2	90	180	310	590	1900
Laser power (W)	0.6	1.43	3.26				
	0.9		3.22				
	1.2	1.85	5.15	3.85	2.34	2.23	2.35
	1.4	1.60	3.22	2.85	3.14	3.08	4.65
	1.6	2.88	3.03	3.20		2.75	3.75
	3.1		3.45				

The as-deposited film composition is strongly dependent on both laser power and deposition pressure. For low pressure depositions (2 mTorr), the M:Te ratio is close to twice that of the target value, indicating either the presence of excess metal atoms or loss of Te. High M:Te ratios are also seen for high deposition pressures and low laser powers. These samples also generally exhibit low values of Sb:Bi. Films closest in composition to the PLD target (M:Te = 0.67, Sb:Bi = 3) are obtained with intermediate deposition pressures (90 and 180 mTorr) and laser powers (1.2–1.6 W).

The room temperature electrical conductivity, Seebeck coefficient and power factor for several members of this set of films were characterized. The electrical conductivity increases significantly with decreasing deposition pressure: conductivities of 5×10^3 – 5×10^4 S/m were recorded for films deposited at 2 mTorr, 50–250 S/m for films deposited at 90 and 180 mTorr, and 1–200 S/m for films deposited at pressures higher than 300 mTorr. For a given pressure the conductivity increased with increasing laser power. The measured magnitude of the Seebeck coefficient generally decreased with increasing conductivity (lower deposition pressures and higher laser powers). Interestingly, several films deposited at 2 mTorr exhibit negative Seebeck coefficients (in the range of -40 to -10 μ V/K) while all the films deposited at higher pressure exhibit positive Seebeck values.

The power factor values for these films ranged between 8.7×10^{-6} and 1.2×10^{-4} W/m K². The best power factor value in this set, however, is still ~ 40 times lower than the literature value for Bi_{0.5}Sb_{1.5}Te₃ 4.6×10^{-3} W/m K². The highest power factor values are measured for intermediate gas pressures and laser powers – the same deposition conditions that typically yield films closest in composition to the PLD target. The *n*-type films (deposited at

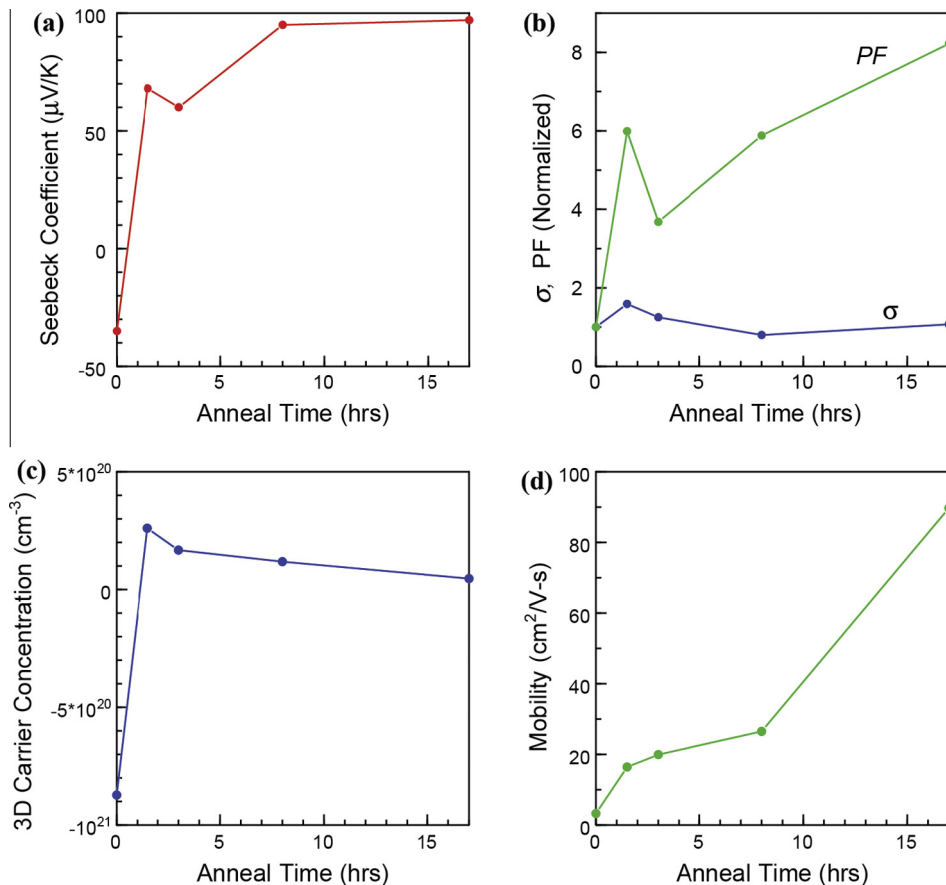


Fig. 8. Transport properties of films deposited at 2 mTorr and annealed in N₂. (a) Seebeck coefficient, (b) electrical conductivity and power factor (normalized to the values measured as-deposited), (c) 3D carrier concentration and (d) Hall mobility as a function of annealing time.

2 mTorr), despite deviating in composition significantly from the target, have power factor values that are not very different than those of the stoichiometric films. These results point to the crucial need for post-deposition annealing for improving the composition, texture and transport properties of pulsed laser deposited $\text{Bi}_{2-x}\text{Sb}_x\text{Te}_3$ films over the entire range of deposition conditions.

3.2. Investigation of annealing conditions

3.2.1. Annealing in nitrogen

Annealing the deposited films in a N_2 atmosphere can potentially promote grain growth, leading to better thermoelectric transport properties. Below we present annealing studies for films deposited at 1.6 W and 2 mTorr for 26 min. We note that annealing of films deposited at higher laser powers and deposition pressures (3.1 W, 90 mTorr and 1.6 W, 180 mTorr) was also investigated. While the crystallinity of these films improved with annealing in N_2 , annealing did not lead to the formation of the alloy phase in these films. XRD results always indicate the presence of two separate Bi_2Te_3 -rich and Sb_2Te_3 -rich phases. Further, the compositions of the films deposited with these conditions actually get worse (further from the target stoichiometry) with annealing. It is therefore not surprising that no significant improvement in the power factor values of these films could be achieved by annealing in N_2 .

The values of the Seebeck coefficient for the set of N_2 -annealed films are shown as a function of annealing time in Fig. 8(a). The electrical conductivity and power factor values are given (normalized to the values measured as-deposited) as a function of annealing time in Fig. 8(b). While the electrical conductivity is relatively constant, the Seebeck coefficient improves by a factor of nearly 3 with annealing. This leads to a >8-fold increase in the power factor value with 17 h annealing. Measured values of the carrier

concentration and Hall mobility are given as a function of annealing time in Fig. 8(c and d), respectively. With annealing, the magnitude of the carrier mobility increases by a factor of 30 while the carrier concentration changes sign and decreases by a factor of 20.

The XRD spectra for this set of films are compared in Fig. 9. With N_2 annealing, the film transforms from a disordered structure, exhibiting several broad peaks, into a crystalline and highly textured structure, exhibiting exclusively high-intensity (00 l) family peaks. The structural transformation is evident from changes in the peaks near 19° and 47° : these peaks narrow and shift to lower angles (higher lattice constants) with annealing. After 17 h annealing, these peaks are aligned with expected (006) and (0015) reflections for the alloy. We note that this does not occur for the (009) and (0018) peaks, which maintain the same width and shift to higher angles with annealing.

The improved crystallinity of the films with annealing can also be seen in top-surface SEM images (Fig. 10). As-deposited, the films are smooth and grain boundaries are difficult to resolve (see image for 1.6 W, 2 mTorr deposition conditions in Fig. 5). With annealing, grain boundaries are visible and the grain size increases with the length of the anneal. After 17 h annealing, the grains are highly faceted (many exhibiting a hexagonal shape) and plate-like, parallel to the substrate.

For films annealed in N_2 for more than 1.5 h, the XRD spectra indicate the presence of a single phase, identified as the $\text{Bi}_{2-x}\text{Sb}_x\text{Te}_3$ alloy. The exact composition of the $\text{Bi}_{2-x}\text{Sb}_x\text{Te}_3$ alloy is difficult to determine from the XRD results, even for the highly textured 17 h-annealed sample. This is because, the c lattice parameters for Bi_2Te_3 and Sb_2Te_3 are nearly identical (varying by only 0.4%), and the value of c for the alloy is not well-established.

The change in composition with N_2 annealing helps to shed light on the structural transformation suggested by Fig. 9. The

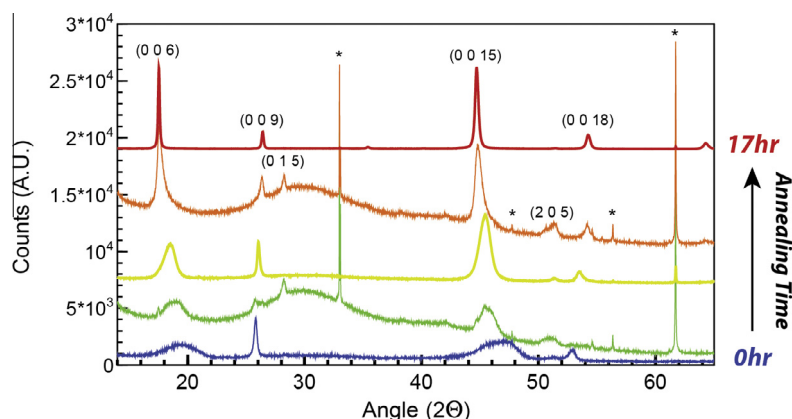


Fig. 9. XRD spectra for films annealed in N_2 between 0 and 17 h. Annealing time increases from blue to red (bottom to top). The traces were scaled and offset to depict time evolution. Several $\text{Bi}_{2-x}\text{Sb}_x\text{Te}_3$ peaks (JCPDS 072-1836) are labeled. Peaks from the Si substrate are marked by *. (For interpretation of the references to color in this figure legend, the reader is referred to the web version of this article.)

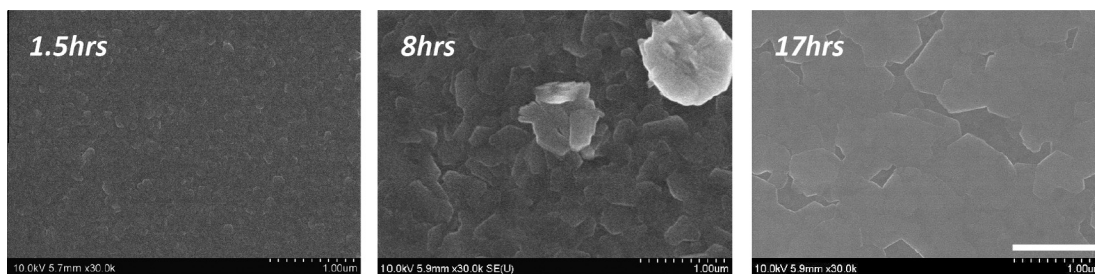


Fig. 10. SEM images of films annealed under N_2 for 1.5, 8 and 17 h. All images were taken at a magnification of 30kx. Scale bar: 1000 nm.

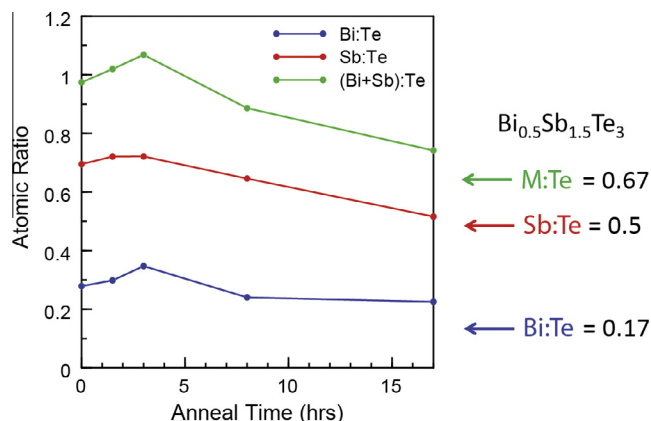


Fig. 11. Atomic ratios (measured using ICP-OES) as a function of annealing time. Target values are indicated by arrows on the right.

atomic ratios Bi:Te, Sb:Te and M:Te measured with ICP-OES are given as a function of annealing time in Fig. 11. As-deposited, the films contain excess Sb and Bi. With annealing, the Bi:Te, Sb:Te and M:Te ratios decrease down to the target value. The ratio of Sb to Bi (not shown) is relatively constant at ~ 2.5 for the entire range of annealing times, indicating that Sb and Bi are maintained in the film during the N_2 annealing or are lost at approximately the same rate.

The structural characteristics of Bi-rich phases of the Bi–Te system have been investigated recently by several groups [13,17–19]. The range of layered compounds between pure Bi and Bi_2Te_3 are part of a homologous series $(Bi_2)_m(Bi_2Te_3)_n$; all known intermediate phases (including Bi_4Te_3 and $BiTe$) can be understood as stacks of Bi_2 blocks sandwiched between blocks of Bi_2Te_3 . A similar series of phases has been demonstrated for the Sb–Te system [20]. Though to our knowledge no such investigation has been performed on the alloy (Bi,Sb)–Te, the layered structure of the (Bi,Sb)–Te system is the same as that of Bi–Te and Sb–Te. The structural transformation in our films with annealing (Fig. 9) is therefore understood as a transition from a disordered metal-rich phase (potentially $Bi_{1-x}Sb_xTe$ or $Bi_{4-x}Sb_xTe_3$) into the phase of the target, $Bi_{2-x}Sb_xTe_3$. At this time, it is unclear what the source of the disorder is (nanoscale grains, variation in the lattice constant, the presence of multiple phases, misaligned layers, etc.). Further investigation of the disordered films by Raman spectroscopy could shed light on this question [17].

The change in transport properties with annealing (reported in Fig. 8) can therefore be understood as the result of both grain growth as well as a change in material (from a disordered metal-rich phase into the stoichiometry of the target). The transport results further support the proposed structural transformation described above: Russo et al. [17] reported that the metal-rich phases of Bi–Te exhibit significantly lower magnitudes of the Seebeck coefficient and mobility, and higher carrier concentrations.

The results described in this section indicate that annealing films under N_2 leads to better crystallinity and better stoichiometry in the $Bi_{2-x}Sb_xTe_3$ pulsed laser deposited films (grain growth, and the formation of the target $Bi_{2-x}Sb_xTe_3$ phase). As a result, the power factor values increase with annealing. However, the highest power factor value achieved after annealing for 17 h is still almost an order of magnitude lower than the literature value. In the next section, we explore the effect of annealing under a Te vapor to further improve the power factor values.

3.2.2. Annealing in tellurium vapor

Loss of Te in Bi_2Te_3 -based nanostructures can lead to deterioration in the thermoelectric transport properties. One technique

developed to resolve this issue is to anneal the nanostructures in a Te vapor (as opposed to an inert gas). This idea was originally proposed by Taylor et al. in 2010, and was shown to yield excellent control over the composition and carrier concentration of thermally evaporated Bi–Te thin films [21]. Improvements of 50% in the Seebeck coefficient were demonstrated after just 60 min annealing in a Te vapor. Similar results have since been reported for electrochemically deposited Bi_2Te_3 [22], $Bi_{2-x}Sb_xTe_3$ and $Bi_2(Te_xSe_{1-x})_3$ [23] thin films. The results of the former study indicate that the Seebeck coefficient of Bi-rich films increases by as much as 300% as the composition becomes stoichiometric with annealing. Interestingly, Te vapor annealing was beneficial both for Bi-rich and Te-rich compositions, indicating that the annealing does not result in excess incorporation of Te even for long anneal times.

In the cited works, vapor annealing of the samples was done in evacuated glass ampoules containing powder Te sources. With our co-deposition system, annealing in Te vapor can be done in the chamber immediately after pulsed laser deposition using the thermal evaporation module. We focus on the effect of annealing metal-rich films deposited on (100) Si with a laser power of 1.6 W at a background pressure of 2 mTorr. The films were annealed with continuous Te evaporation (for up to 22 h), after which the pressure was increased to 2 Torr for cooling.

The XRD spectra for several films annealed in Te vapor are shown in Fig. 12. These results indicate the same transformation from disordered to textured morphologies with annealing (compare with Fig. 9). Further, despite the large quantities of Te evaporated (ex: assuming a rate of 0.01 Å/sec, we could expect a thickness of 47 nm evaporated Te on the substrate), no separate crystalline Te peaks are seen in the XRD spectra. Throughout the annealing process, the Te is completely incorporated into the film or pumped away. In a control experiment, the PLD step was skipped, and annealing of the bare Si substrate resulted in no Te deposition. Naturally, tellurium was found to accumulate in colder sections of the vacuum system.

The compositions of the Te annealed films were measured by ICP-OES. The measured ratios (Bi + Sb):Te are shown as a function of annealing time in Fig. 13(a). The power factor values measured for the same set of samples are shown in Fig. 13(b). In general, the M:Te ratio approaches the target value of 0.67 and the power factor increases with annealing time (the rates of change for the M:Te atomic ratios and the power factor are given in Table 5). However, it is important to note the significant scatter in M:Te ratios and power factor values in the sample set. The power factor values (shown in Fig. 13(b)) range between 1×10^{-5} W/m K² and

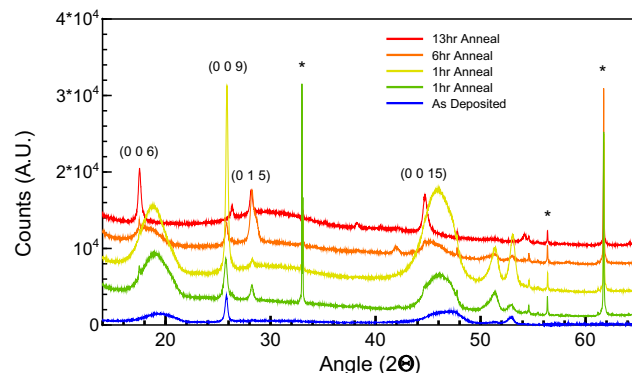


Fig. 12. XRD spectra for several films annealed in Te vapor (1–13 h) compared with the spectrum from a film as-deposited. The traces were offset vertically to depict time evolution. Several high-intensity $Bi_{2-x}Sb_xTe_3$ peaks are marked. Peaks from the Si substrate are marked by *.

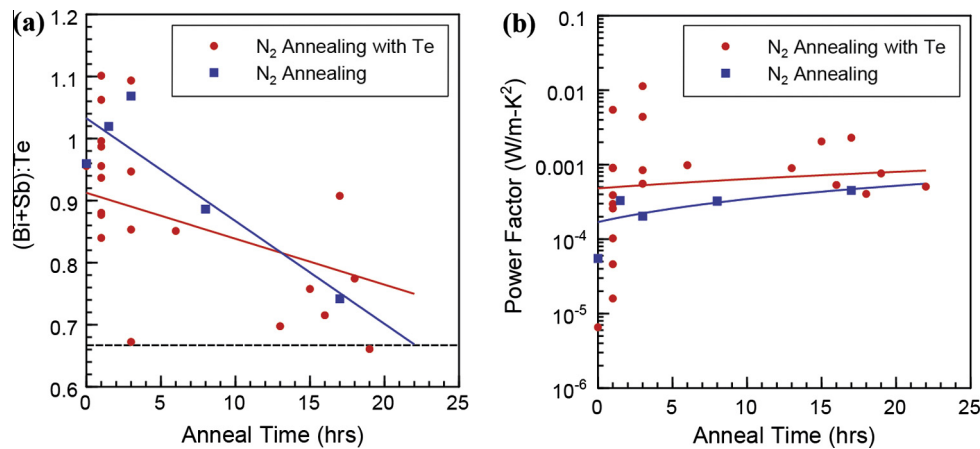


Fig. 13. (a) Metal-to-tellurium atomic ratio (measured using ICP-OES) as a function of annealing time. Results for films annealed in Te vapor (red circles) are compared with those for films annealed in N₂ (blue squares). The stoichiometric ratio of the target is marked by a dashed horizontal line. (b) Power factor values as a function of annealing time for the same set of samples. (For interpretation of the references to colour in this figure legend, the reader is referred to the web version of this article.)

Table 5

Rates of change in the M:Te atomic ratios and the power factor values with annealing in N₂ with a Te vapor, and annealing in N₂. These values correspond to the slope of the lines in Fig. 13.

Annealing conditions	d(M:Te)/dt (1/h)	d(PF)/dt (W/m K ² -h)
N ₂ annealing with Te	$-0.76 \times 10^{-2} \pm 0.22 \times 10^{-2}$	$1.4 \times 10^{-5} \pm 1.1 \times 10^{-5}$
N ₂ Annealing	$-1.7 \times 10^{-2} \pm 0.48 \times 10^{-2}$	$1.75 \times 10^{-5} \pm 0.75 \times 10^{-5}$

$11.3 \times 10^{-3} \text{ W/m K}^2$ – the high end value is 2.5 times the bulk value.

Annealing under Te vapor leads to higher power factor values than annealing in N₂; however, the results in Fig. 13 indicate that the power factor values are spread over a large range and are generally still lower than that of bulk. Interestingly, measurements on 3 of the films resulted in power factors equal or larger than bulk. It is not yet clear from the analysis of crystal structure or composition what distinguishes the films with high power factor values ($>4 \times 10^{-3} \text{ W/m K}^2$) from the rest of the samples. In general, higher Te evaporation rates and short annealing times (1.5–3 h) appear to have led to the higher power factor values.

4. Summary

An investigation of the effect of various deposition conditions (substrate temperature, laser power, background pressure) on the properties of Bi_{2-x}Sb_xTe₃ films deposited via PLD was presented. A relatively high substrate temperature is required to yield conducting films. The films closest to the target composition are deposited for intermediate values of the laser power ($\sim 1.4 \text{ W}$) and background pressure ($\sim 180 \text{ mTorr}$). If the pressure is above 2 mTorr, however, the deposited film contains separate Bi₂Te₃ and Sb₂Te₃ phases and occasionally crystalline Te.

Films deposited with a laser power of 1.6 W and a pressure of 2 mTorr were the focus of an annealing study. As-deposited, these films consist of a metal-rich non-stoichiometric phase with structural disorder and can exhibit small negative Seebeck coefficients. With annealing in N₂, the films become crystalline (reverting to the M:Te 2:3 stoichiometry of the target) and highly textured (with strong (001) diffraction peaks). This improvement in crystallinity is accompanied by decreases in the carrier concentration and increases in the mobility. While annealing leads to a change in

both the sign (from n-type to the expected p-type) and the magnitude (3-fold increase) of the Seebeck coefficient, the electrical conductivity remains nearly constant. The result is a factor of more than 8 improvement in the power factor value.

Finally, we investigated the effect of annealing the films in Te vapor in the PLD-TE chamber immediately after film deposition. The power factor of films annealed in a Te vapor is larger than that of films annealed in N₂, with several films showing power factor values comparable to or higher than the bulk value. Since the thermal conductivity is expected to be no larger than that of bulk, ZT values of these films can be exceptionally high. Additional work is required to improve control over the annealing process, aimed at minimizing the variation of thermoelectric transport results from run to run.

Acknowledgements

This work was supported by the Minta Martin Foundation. J.E.C. acknowledges an Achievement Rewards for College Scientists Foundation scholarship. The support of the Maryland NanoCenter and its Nisplab is appreciated. The Nisplab is supported in part by the NSF as an MRSEC Shared Experimental Facility.

References

- [1] Noh HJ, Koh H, Oh SJ, Park JH, Kim HD, Rameau JD, et al. Spin-orbit interaction effect in the electronic structure of Bi₂Te₃ observed by angle-resolved photoemission spectroscopy. *Europhys Lett* 2008;81:57006.
- [2] Rowe DM. In: *Thermoelectrics Handbook: Macro to Nano*. CRC Press; 2006.
- [3] Smith MJ, Knight RJ, Spencer CW. Properties of Bi₂Te₃-Sb₂Te₃ alloys. *J Appl Phys* 1962;33:2186–90.
- [4] Bekebrede WR, Guentert OJ. Lattice parameters in the system antimony telluride bismuth telluride. *J Phys Chem Solids* 1962;23:1023–5.
- [5] Birkholz U. Untersuchung Der Intermetallischen Verbindung Bi₂Te₃ sowie Der Festen Lösungen Bi_{2-x}Sb_xTe₃ Und Bi₂Te₃-Sb₂Te₃ Hinsichtlich Ihrer Eignung Als Material Für Halbleiter-Thermoelemente. *Zeitschrift Für Naturforschung Part a-Astrophysik Physik Und Physikalische Chemie* 1958;13:780–92.
- [6] Ashcroft NW, Mermin ND. *Solid state physics*. Holt, Rinehart and Winston; 1976.
- [7] Tritt TM. *Thermal Conductivity: Theory, Properties, and Applications*. Springer; 2004.
- [8] Goldsmid HJ, Sheard AR, Wright DA. The performance of bismuth telluride thermojunctions. *Br J Appl Phys* 1958;9:365–70.
- [9] Drašar C, Steinhart M, Lošťák P, Shin HK, Dyck JS, Uher C. Transport coefficients of titanium-doped Sb₂Te₃ single crystals. *J Solid State Chem* 2005;178:1301–7.
- [10] Wright DA. Materials for direct-conversion thermoelectric generators. *Metall Rev* 1970;15:147–60.
- [11] Dauscher A, Thomy A, Scherrer H. Pulsed laser deposition of Bi₂Te₃ thin films. *Thin Solid Films* 1996;280:61–6.

- [12] Bailini A, Donati F, Zamboni M, Russo V, Passoni M, Casari CS, et al. Pulsed laser deposition of Bi_2Te_3 thermoelectric films. *Appl Surf Sci* 2007;254:1249–54.
- [13] Li Bassi A, Bailini A, Casari CS, Donati F, Mantegazza A, Passoni M, et al. Thermoelectric properties of Bi–Te films with controlled structure and morphology. *J Appl Phys* 2009;105:124307.
- [14] Makala RS, Jagannadham K, Sales BC. Pulsed laser deposition of Bi_2Te_3 -based thermoelectric thin films. *J Appl Phys* 2003;94:3907–18.
- [15] Obara H, Higomo S, Ohta M, Yamamoto A, Ueno K, Iida T. Thermoelectric properties of Bi_2Te_3 -based thin films with fine grains fabricated by pulsed laser deposition. *Jpn J Appl Phys* 2009;48:085506.
- [16] Nolas GS, Sharp J, Goldsmid J. *Thermoelectrics: basic principles and new materials developments*. Springer; 2001.
- [17] Russo V, Bailini A, Zamboni M, Passoni M, Conti C, Casari CS, et al. Raman spectroscopy of Bi–Te thin films. *J Raman Spectrosc* 2008;39:205–10.
- [18] Bos J, Zandbergen H, Lee MH, Ong N, Cava R. Structures and thermoelectric properties of the infinitely adaptive series $(\text{Bi}_2)_m(\text{Bi}_2\text{Te}_3)_n$. *Phys Rev B* 2007;75.
- [19] Hsin C-L, Wingert M, Huang C-W, Guo H, Shih T-J, Suh J, et al. Phase transformation and thermoelectric properties of bismuth-telluride nanowires. *Nanoscale* 2013;5:4669–72.
- [20] Poudeu PFP, Kanatzidis MG. Design in solid state chemistry based on phase homologies. Sb_4Te_3 and Sb_8Te_9 as new members of the series $(\text{Sb}_2\text{Te}_3)_m(\text{Sb}_2)_n$. *Chem Commun* 2005;21:2672–4.
- [21] Taylor A, Mortensen C, Rostek R, Nguyen N, Johnson DC. Vapor annealing as a post-processing technique to control carrier concentrations of Bi_2Te_3 thin films. *J Electron Mater* 2010;39:1981–6.
- [22] Rostek R, Sklyarenko V, Woias P. Influence of vapor annealing on the thermoelectric properties of electrodeposited Bi_2Te_3 . *J Mater Res* 2011;26:1785–90.
- [23] Schumacher C, Reinsberg KG, Rostek R, Akinsinde L, Baessler S, Zastrow S, et al. Optimizations of pulsed plated p and n-type Bi_2Te_3 -based ternary compounds by annealing in different ambient atmospheres. *Adv Energy Mater* 2013;3:95–104.